UNIVERSITY OF OKLAHOMA

GRADUATE COLLEGE

AN ANALYSIS OF THE MICROPHYSICAL AND THERMODYNAMIC PROPERTIES OF ELEVATED CONVECTIVE CELLS WITHIN SNOWBANDS ASSOCIATED WITH WINTER STORMS.

A THESIS

SUBMITTED TO THE GRADUATE FACULTY

in partial fulfillment of the requirements for the

Degree of

MASTER OF SCIENCE

By

Christian Hall
Norman, Oklahoma
2023

AN ANALYSIS OF THE MICROPHYSICAL AND THERMODYNAMIC PROPERTIES OF ELEVATED CONVECTIVE CELLS WITHIN SNOWBANDS ASSOCIATED WITH WINTER STORMS.

A THESIS APPROVED FOR THE
SCHOOL OF METEOROLOGY

BY THE COMMITTEE CONSISTING OF

Dr. Greg McFarquhar, Chair

Dr. David Schvartzman

Dr. Cameron Homeyer

Acknowledgements

I would like to thank Dr. Greg McFarquhar for helping to sustain and guide this research, my graduate committee for their input, and the School of Meteorology at the University of Oklahoma for the opportunity to attend graduate school. This work was funded by the NASA Earth Venture Suborbital-3 (EVS-3) program under Grant 80NSSC19K0399 (OU).

Contents

Abstract

In-situ and remote sensing observations of snowbands were obtained by probes on a cloud-penetrating NASA P-3 and a high-altitude NASA ER-2 aircraft, to identify and characterize elevated convective cells (CCs). Observations were made during the Investigation of Microphysics and Precipitation for Atlantic Coast-Threatening Snowstorms (IMPACTS) field campaign in 2020. The radar reflectivity and Doppler velocity measured by a Cloud Radar System (CRS) on the ER-2 were used to identify CCs for time periods when the horizontal separation between the ER-2 and the P-3 was less than 1.4 km, with the characteristics of small-scale air motion subsequently determined by the Turbulent Air Motion Measurement System (TAMMS) on the P-3. Through a case study analysis of collocated regions with radar confirmed CCs, an algorithm that considered the statistical significance of the range in small scale vertical velocity from the TAMMS, as well as the magnitude of the largest velocity, was developed to identify CCs using data exclusively recorded by the TAMMS. Using time periods identified as containing elevated CCs from the TAMMS for the entire 2020 IMPACTS campaign, cloud microphysical properties derived from the Rosemount Icing Detector (RICE), Fast Cloud Droplet Probe (CDP), 2D-S Stereo Probe (2DS), and High-Volume Precipitation Spectrometer (HVPS) installed on the P-3 were used to characterize the cloud microphysical properties inside and between CCs. Cloud penetrations were defined as sequences of 20-second time intervals when the P-3 encountered cloud particles at least once every 6-7 seconds, until there was a gap of at least 6-7 seconds between cloud particles. Of the 94 instances of cloud penetration identified from the P-3 analysis, 29 contained at least one CC. Contrary to previous observations of convective cells such as in generating cells in winter storms, distributions of IWC and mass-weighted mean particle dimension were not statistically different for data collected within and

between CCs. However, mean number-weighted particle dimensions were 0.35 mm larger between CCs than within. Total number concentrations and LWC averaged 2.8 times larger and 2.3 times larger, respectively, within CCs than between. Temperatures were on average 2.4 °C greater, and dewpoint depressions 0.77 °C smaller within CCs than between. There was a 9% decrease in supercooled liquid water (SLW) presence between CCs compared to within, and SLW was detected within all TAMMS confirmed CCs. The means for defining CC regions in a substantiated way with in-situ measurements depends on the reliability of contrasting data recorded from the ER-2 and P-3 aircraft during collocated time periods, as well as the number of collocated time periods available. It is because of these limitations, and the unconventional means for detecting CCs using the TAMMS, that differences in the observed characteristics of TAMMS-confirmed CCs may be present when compared to previous studies.

1. Introduction

a. Purpose

Snowstorms on the eastern seaboard persistently threaten disruptions to transportation, commerce, and public safety. The snow in these storms can often be seen organized into banded structures that are unpredictable and under-studied. Specifically, causes of banded reflectivity patterns and isolated cellular convection in winter storms are some of the most important processes to consider when trying to predict the variability in location, type, and intensity of winter precipitation (Rosenow et al. 2014). The technology available to research scientists, including advancements in remote sensing and numerical weather prediction capabilities, has improved significantly since the last major study on eastern seaboard snowstorms, which took place over thirty years ago. A new study on these storms of a significant magnitude was long overdue. During January and February of 2020, The Earth Science Project Office (ESPO) at The National Aeronautics and Space Administration (NASA) conducted the first phase of the Investigation of Microphysics and Precipitation for Atlantic Coast-Threatening Snowstorms (IMPACTS; McMurdie et al. 2022) field campaign to study winter snowstorms on the eastern seaboard. However, due to the lack of snowstorms along the eastern seaboard that year, IMPACTS sampled snowstorms over a much broader area than originally anticipated with sampling as far west as Illinois. Thus, analysis of IMPACTS data encompasses a broader range of longitudes.

Data collected during IMPACTS considerably enhances previously available data acquired during the Profiling of Winter Storms (PLOWS; Rosenow et al. 2014; Market et al. 2012) project, which was a two-year field campaign completed during the 2008-2009 and 2009-2010

winter seasons. PLOWS examined the microphysical and dynamical properties of the comma-head region of continental winter storms that drives the variability of precipitation within these storms. IMPACTS differed from PLOWS in that it was developed to study winter storms along the eastern seaboard, and it had a more comprehensive array of remote sensing instrumentation. It is important to study winter cyclones that originate from the North-East as a separate entity due to their unique tendencies to undergo rapid cyclogenesis, making them harder to predict. The Solid Precipitation Intercomparison Experiment (SPICE; Smith et al. 2020) focused on improving quantitative estimates of snowfall from winter storms, while the primary focus of IMPACTS was on the microphysical components of the banded structure embedded within snowstorms and their associated precipitation. The Southern Ocean Clouds Radiation Aerosol Transport Experimental Study (SOCRATES; Marchand et al. 2014) sampled the nature of clouds over the Southern Ocean with the ultimate goal of improving climate models that take them into consideration. SOCRATES also conducted research on the microphysical structure of these clouds in and between regions of cellular convection (Wang et al. 2020). An objective of IMPACTS was to analyze similar regions of elevated convection, but within the winter storms as previously mentioned along the eastern seaboard. However, given the data obtained during IMPACTS 2020, analysis of elevated convection in multiple geographic regions was possible.

b. Background

Typically observed by radar, generating cells (GCs) are a specific type of elevated convective cell (CC) located near the top of a cloud, typically consisting of a 1-2km wide region of locally high reflectivity from which a trail of hydrometeors emanates. It has been postulated that snow crystals are formed and grow in GCs, and that the cells are subsequently maintained by convection induced by the release of latent heat accompanying crystal growth (Marshall 1953;

Wexler and Atlas 1959). The shape of the snow trail below a GC depends on the fall speed of the snow and the vertical profile of the horizontal wind (AMS 2022). While the dynamical properties of GCs and CCs are similar (Murphy et al. 2017), the defining features of GCs are their elevation relative to cloud-top and their precipitation fall streaks. Elevated cellular convection not associated with GCs is characterized by a ~5 km deep tower of convection with cloud particles distributed evenly throughout their depths (Rosenow et al. 2014), and is frequently associated with large-scale or meso-scale features. While they are a type of isolated elevated convection, GCs typically exist as smaller cells atop a layer of stratiform cloud characterized by slanted fall streaks of precipitation below. Various studies have been done, some of which were associated with the research campaigns already mentioned, to identify these elevated regions of reflectivity and convection as well as characterize them in terms of their microphysical and dynamical structure. While the literature pertaining to the analysis of GCs is limited, even more limited analyses exist for characterizing CCs in winter snowstorms. Thus, previous studies identifying and characterizing GC microphysical properties serve as a useful basis for characterizing and analyzing elevated convection, where elevated convection can be identified without the restriction of being near cloud top or having emanating precipitation fall streaks.

i. GC characteristics

GCs have been observed to have relatively consistent spatial dimensions. Widths are mostly on the order of 1 km, with vertical thicknesses up to 1 km as well (Kumjian et al. 2014). Although there is some variability in the microphysical properties of GCs, even within similar temperature and elevation ranges, in general, the fall-streaks emanating from GCs have more pronounced reflectivity and Doppler velocities (Kumjian et al. 2014). Kumjian et al. (2014) provided a comprehensive summary of nearly a dozen studies of GCs that suggest unstable air

near cloud-top drives the convective instability responsible for producing them and their associated precipitation fall-streaks. A notable exception, however, is the study of Ludlam (1956), that suggested that the convection associated with GCs is initiated by the latent heat released by the formation and growth of ice crystals.

GCs have been mostly observed near cloud-top at heights ranging from 3 to 8 km and temperature levels from -12 °C to less than -40 °C. Updraft speeds have been consistently reported to be around 1 ms^{-1} (Kumjian 2014). Kumjian et al. (2014) found that GCs are very common in snowstorms, primarily located in deeper clouds. In preceding studies such as Douglas (1957), there was no preferred altitude or temperature level that harbored GCs in winter storms, which suggests that they can be encountered even below cloud top as moist parcels of air rise through stratiform cloud particles. These GCs below cloud top could consequently be considered to be CCs that contain more enhanced microphysics with larger particle diameters.

Wang et al. (2020) identified GC locations using remote sensing radar reflectivity and simultaneous vertical velocity measurements from the HIAPER Cloud Radar (HCR), while in-situ measurements allowed for comparison of microphysical properties inside and outside radar-confirmed GCs. Although a prominence of radar reflectivity greater than 4 dBZe was primarily used to identify GCs, the velocity of a peak in upward vertical motion must have been larger than the 25th percentile of the distribution of velocity across the entirety of the cloud to avoid identifying small peaks in reflectivity (Z_e) that were not accompanied by rising motion. In midlatitude winter cyclones, Plummer et al. (2014) located GCs using measurements of radar reflectivity obtained by an aircraft equipped with probes for in-situ measurements. All points within ± 2 s of flight time of 4-dB local Z_e maxima measured across the breadth of the cloud by the Wyoming Cloud Radar (WCR) were assumed to be within GCs. To quantify the

microphysical properties of GCs, Wang et al. (2020) determined cloud phase as either liquid, ice, or mixed phase for every second of flight time by first using the RICE probe to detect supercooled liquid water (SLW) for temperatures less than -4 °C during changes in voltage of at least 2 mV s^{-1} (Cober et al. 2001). The 2D-S probe was used to identify the presence of ice particles when the total number concentration of particles with maximum dimensions larger than 200 μm was greater than 0 L^{-1}. N(D) of SLW droplets ranging from 2 μm to 50 μm in diameter was determined from the CDP measurements following McFarquhar et al. (2007, 2011) and McFarquhar & Cober (2004)'s assumption that any small particles in mixed-phase clouds were likely to be SLW droplets. The primary limitation of the Wang et al. (2020) study was that the HCR had a dead zone of 145 m where measurements of reflectivity and vertical velocity were not available, meaning there was a spatial separation between the remote sensing data and the in-situ measurements. Nevertheless, it has been established that SLW occurs in GCs. The simultaneous occurrence of ice in GCs suggests they provide a protective environment for the formation and growth of ice crystals (Wang et al. 2020).

Observations from Kumjian et al. (2014) suggest that dendrites are frequently present in mature GCs with higher supersaturations, while small platelike crystals are present in weaker GCs with smaller supersaturations. They proposed that the microphysical structure of GCs is predominantly governed by the temperature level at which they form. Plummer et al. (2014) showed that within GCs, the median and 95th percentile SLW content measured at temperatures between -31.4 °C and -11.1 °C increased from ~0.09 g m^{-3} to 0.12 g m^{-3} and ~0.14 g m^{-3} to 0.28 g m^{-3}, respectively, with SLW present in 26% of the observations within GCs and 18% of the observations between GCs. Once the convection associated with GCs has been initiated, ice nucleation and growth are largely dependent on said convection to a certain point, after which

the ice crystals will fall below the GCs and continue their growth through riming and aggregation (Plummer et al. 2015). Wang et al. (2020) detected SLW in all measured GCs with an average liquid water content (LWC) of 0.31 ± 0.19 g m^{-3}, 11% larger than LWCs between GC. The difference in the number concentration of cloud droplets with a maximum dimension of 50 μm or smaller inside and between GCs was insignificant. On the other hand, Plummer et al. (2014, 2015) showed ice particle concentrations 1.9 times larger within GCs than between them, as well as ice water content (IWC) measurements and median mass diameters (MMDs) 2.2 and 1.1 times larger within GCs, respectively. The growth of ice crystals occurring as they rise and fall within GCs was presented as the primary mechanism for ice crystal maturation. In Wang et al. (2020), MMD values above 200 μm were 37% more frequent inside GCs than between.

ii. CC characteristics

CCs differ from GCs in that they primarily exist in the stratiform region below cloud-top. More limited studies exist on the in-situ microphysical characteristics of elevated CCs than of GCs. Thus, algorithms to identify CCs must be based primarily on their dynamical rather than microphysical properties. In a study of elevated convection in the comma-head region of winter cyclones (Murphy et al. 2017), elevated CCs were identified as distinct towers of enhanced reflectivity and vertical air motion with an absence of generating cells at the top of the tower. The residual stratiform regions left behind by convective cells were assumed to have a different microphysical structure than those of stratiform regions generated by synoptic scale lifting. Doppler velocities varied between -3 and 5 ms^{-1} at the altitudes where CCs resided. Updrafts, downdrafts, and residual stratiform rising within regions of convection were defined in terms of vertical air motion as $W > 1$ ms^{-1}, $W < 1$ ms^{-1}, and -1 $ms^{-1} < W < 1$ ms^{-1} respectively. Murphy et al. (2017) determined that turbulence within CCs was responsible for mixing of ice particles

throughout their depths, producing a pseudo-uniform particle size distribution. The average width to depth ratio was relatively uniform; discrete elevated cellular convection had vertical and horizontal scales of approximately 5 km (Rosenow et al. 2014). Rosenow et al. (2014) and Cronce et al. (2007) found that the vertical velocity values in the core of elevated convective cells were as high as around 7 ms^{-1} while the periphery of the cores had negative values as low as -4 and -5 ms^{-1}. SLW, as well as ice particles and graupel, has been indicated to occur in CCs within sampled winter storms, as well as ice particles and graupel (Rauber et al. 2014). It is postulated that these regions of convection, like GCs, provide the upward air motion required for the formation and growth of these larger ice particles and supercooled liquid water droplets (Rauber et al. 2014). Murphy et al. (2017) showed that the distribution of IWC and MMD values throughout CCs was indistinct, suggesting that vertical mixing in these cells distributes particles throughout space. Decreases in IWC with increasing MMD below cloud-top in residual stratiform regions were explained by particles falling and aggregating as entrainment-forced sublimation of ice content (Wexler, 1955).

While GCs and CCs have differences, Rosenow et al. (2014) showed that they can be studied using similar dynamical identification criteria. During IMPACTS, cloud top height was frequently well above the altitude of the P-3 equipped with the in-situ probes. Additionally, the product of cloud top height was highly dependent on the radar frequency and wavelength utilized in analysis. Due to this restraint, it was difficult to identify the observed convective cells as examples of GCs. Therefore, the isolated regions of elevated convection identified and measured in this study are more generally referred to as elevated convective cells (CCs). Nevertheless, the collocation of data from in-situ and remote sensing instruments during IMPACTS that measure both dynamics and microphysics of CCs simultaneously considerably extends previously

available observations, so that the context of the observed microphysical properties in terms of the motion producing those properties is better understood. One-second temporal resolution was used to characterize the microphysical properties of CCs given their horizontal variability, even though longer averaging periods could be optimal for obtaining more statistically significant measurements (McFarquhar et al., 2007).

c. Research goals

First, broad statistical observations were made to determine a general relationship between the dynamic and microphysical properties of cloud samples taken during the 2020 IMPACTS campaign. Remote sensing data were then used to identify and verify the existence of CCs. Subsequently, in-situ air motion measurements were analyzed to develop an algorithm for identifying CCs without the need for remote sensing. Using an expanded definition of CCs in terms of fine scale, directly measured dynamical properties, the microphysical characteristics of CCs across a selection of data where only in-situ cloud measurements were utilized were extracted. The main scientific questions investigated in this study are thus as follows. *What are the small-scale, in-situ measured, dynamical properties of CCs in banded regions confirmed by remote sensing? Can they be used to develop an algorithm that properly identifies CCs without the need for remote sensing data? What microphysical and thermodynamic characteristics are prevalent within winter storm CCs compared to characteristics outside of CCs?*

2. IMPACTS overview

a. Logistics

IMPACTS flew a combination of remote sensing and in-situ instruments mounted aboard the high-altitude ER-2 and the cloud-penetrating P-3 research aircraft respectively. The P-3 aircraft

was stationed at Wallops Island Flight Facility located on the Eastern Shore of Virginia. During 2020, the ER-2 was stationed out of Hunter Army Airfield in Savanah, GA. The capstone objectives of this field campaign were to provide observations critical to understanding the mechanisms of snowbands formation and evolution to examine microphysical characteristics and growth mechanisms of snow particles across these snowbands, and to improve snowfall remote sensing interpretation and modelling to advance predictive capabilities (McMurdie et al. 2022). On select portions of flights when both aircraft flew, the ER-2 and P-3 executed racetrack patterns as illustrated in Figure 1, favoring locations where precipitation bands were present as originally identified by forecast models, and later augmented by ground-based radar, rawinsonde data, and multiple NASA and NOAA satellites.

Whenever possible, the aircraft flew coordinated in a vertically aligned formation, which will be referred to as "collocation." Each day of data collection featured several distinct straight and level flight legs. It was during these flight legs that brief periods of collocation between the aircraft were attempted. One major challenge in coordinating flight legs between the two aircraft was that the ER-2 has a standard flight speed of around 200 ms^{-1} while the P-3 cruises at ~160 ms^{-1}, with the ground speed varying depending on the speed and direction of the flight level winds. Thus, while speeds fluctuated throughout the flight, the ER-2 travelled significantly longer horizontal distances than the P-3 during the same amount of time. Therefore, the ER-2 legs were longer than the P-3 legs, and coordination was typically obtained at the center point. As a result, periods of collocation began with the ER-2 approaching from behind the P-3. The coordination then ended when the ER-2 was too far ahead of the P-3. This meant that the amount of time that the ER-2 and P-3 were horizontally collocated was limited.

b. Instruments

Not all instruments collected science quality data on every science flight during IMPACTS, so there are moments of discontinuity in select data streams. The times at which high quality remote sensing and in-situ data are available for the instruments used in this study are displayed in Table 1.

i. Turbulent Air Motion Measurement System (TAMMS)

The TAMMS is an in-situ probe installed on the P-3 aircraft during IMPACTS. It utilizes five pressure ports and temperature sensors distributed in a cruciform pattern around the nose of the P-3B radome (Figure 2) that precisely measure three-dimensional air flow relative to the movement of the aircraft and temperature. The P-3 had to be flying consistently between 4 and -4 degrees of pitch and roll in order for the data recorded by the TAMMS to be considered relevant due to the nature of how the instrument records airflow dynamics.

The precise nature of the measurements from the TAMMS was of great importance in this research as one of the primary goals was to contrast the in-situ airflow to the overhead remote sensing measurements of Doppler velocity by the W-band radar aboard the ER-2.

ii. Particle probes

The 2-Dimensional Spectrometer (2DS), High-Volume Precipitation Spectrometer (HVPS3), and Fast Cloud Droplet Probe (FCDP) in-situ particle probes mounted on the P-3 were utilized in this research. The 2DS Stereo Probe is an optical imaging instrument from which the concentration and shape of cloud particles with maximum dimensions (D) between 20 μm and 2 mm can be derived. It obtains cloud particle images from particles shadowing two diode laser beams normal to each other that illuminate two linear 128-photodiode arrays (Lawson et al. 2006). The HVPS-3 utilizes the same mechanism as the 2DS but using one diode laser instead of

two. It was used to sample large volumes of approximately 400 Ls^{-1} of particles normally between 200 μm and 3 mm (McFarquhar et al. 2017) Two HVPS-3 were used during IMPACTS, one mounted horizontally, one mounted vertically. The 2DS and HVPS-3 probes that were utilized resulted in a dataset that separates the horizontal and vertical channels of processed particle information. A product that combined the number distribution function, N(D), derived from the 2DS horizontal channel for 20 μm < D < 2 mm, and from the horizontally mounted HVPS-3 for 200 μm < D < 3 mm was used to characterize N(D) over the complete range of particle sizes. The FCDP uses forward scattering of light from cloud particles to measure particles ranging from 1.5 μm to 50 μm in diameter. Because Mie theory only applies to spherical drops, the FCDP only provides reliable measurements of liquid droplets and not ice crystals. Because of this, the data from the FCDP was used in some portions of this analysis to characterize cloud samples that contained liquid cloud droplets.

iii. Rosemount Icing Detector (RICE)

As ice accumulates on the RICE ice sensor, the frequency of its vibration changes (Cober et al. 2001), which induces a voltage change that signifies the presence of supercooled liquid water (SLW). When the accumulated ice on the RICE vibrating wire exceeds a certain amount, the wire is heated to melt the ice, meaning there is a period of time when the presence of SLW cannot be detected from the RICE probe (Cober et al. 2001).

iv. Cloud Radar System (CRS)

The CRS W-band (94 GHz) fine resolution polarimetric nadir-pointing radar measures reflectivity and Doppler velocity from the high-altitude ER-2 aircraft of the clouds and precipitation below. It sends staggered pulses an average of 2048 times per vertical profile, and has a 0.45-degree beam width. It recorded data at 632 vertical range gates with a 26.25 m

resolution, beginning at 5,014 m away from the radar, for a total vertical range of ≈ 21.6 km (Walker McLinden, et al. 2021). The CRS provided remote sensing data that were used to characterize clouds and precipitation when the ER2 and P-3 were collocated.

3. Methods

The aircraft did not specifically target generating cells, as the cloud tops were frequently too high for the P-3 to reach, or elevated convection during IMPACTS. The main targets of cloud sampling were areas of precipitation banding, typically in the northwest quadrant of cyclones, for temperature ranges where specific microphysical processes were believed to be important, such as secondary ice production, dendritic growth, and aggregation. In this study, CCs were treated as any type of cellular convection, which includes generating cells. So, while the P-3 aircraft did not often pass through cloud-top where GCs exist, they were considered in determining the minimum dimensions to consider for CCs, as GCs are around 1.4 km in maximum width, which is much narrower than the typical width of larger elevated CCs which are not associated with cloud-top particle generation. Additionally, the vertical extent of convective cells and generating cells was not considered when determining an algorithm for their detection, as collocated vertical radar measurements were not readily available for most of the P-3 flights.

a. Broad observations of the in-situ data

An attempt was first made to analyze the breadth of data available from the IMPACTS campaign using bulk parameters. One goal of this study is to compare data from different probes collected on different aircraft during IMPACTS. Thus, a data structure was first generated with elements representing data obtained from each individual probe with only low-quality data removed. General visualizations helped to become familiar with the probe data available and

compare the observations in those visualizations to the understandings of cloud microphysics cultivated by past studies.

i. Time series visualization

A 1-s resolution time series of N(D) measured by the 2DS and HVPS-3 is shown as a color contour plot in Figure 3. Vertical velocity measured by the TAMMS probe is overlaid to illustrate the relationship between N(D) and small-scale air motion. This time period, like many others in this section, was chosen arbitrarily based on the presence of consistent data. A 16-s running time average of the TAMMS vertical velocity showed a general trend of how the vertical air motion is correlated with N(D). There is a higher concentration of particles with $D > 1$ mm when more intense updrafts or downdrafts were seen. From 10:15:45PM to 10:16:15PM UTC, as the vertical velocity rapidly decreased and increased, N(D) for $D < 0.1$ mm decreased from around 200 cm^{-4} to as low as 0.1 cm^{-4}, while N(D) for larger particles $D > 1$ mm increased. Assuming the updrafts and downdrafts shown in Figure 3 during that time were associated with cloud-top cellular convection, this would allow larger particles such as ice crystals and graupel to be present (Rauber et al. 2014). However, the decrease in concentration of smaller cloud particles is inconsistent with the increase in droplet concentrations that Plummer et al. (2014) found within GCs.

A great circle calculation using the Haversine formula and the latitudes and longitudes of both the P-3 and ER2 aircraft was performed to determine the horizontal distance between the planes (Robusto, C. C. 1957). This distance is shown as a function of time in Figure 4 for the 25 January 2020 flight. It was determined that the planes needed to be within 1.4 km to be deemed collocated based on the lower end of the scale for CC dimensions, so that even if a smaller CC,

such as a cloud-top GC, was being measured, both the P-3 and the ER2 were assumed to be measuring the same cell during collocated time periods.

Figure 5 shows a time series indicating whether each time period was in-cloud, out of cloud, whether the aircraft were collocated, whether 1 ms^{-1} updrafts were measured by the TAMMS, and whether or not ice was contained in cloud. This figure shows a period where all IDs were triggered, as an example of a selection of time that would be a good candidate for case study. In-cloud criteria was the presence of either ice water content (IWC) or liquid water content (LWC), and N(D) greater than 0 for particles D > 20 μm. IWC was calculated by a summation of concentrations per size bin across all size bins for ice particles, multiplied by particle mass (M) estimated by $M = 0.0061 * D^{2.05}$. The criteria for ice-clouds were the presence of IWC, and N(D) greater than 0 for particles D > 20 μm. Similar plots for other time periods during IMPACTS allowed identification of sections of time across all flights to be considered for case studies in this research. Overall, sections of time within cloud were almost always accompanied by the presence of ice cloud. This might be reasonable depending on the meteorology sampled on a given day. Regions with updrafts of greater than 1 ms^{-1} were used to identify periods of broad convection, or brief instances where positive vertical velocity was present, that may be associated with CCs. Time periods where all four IDs were triggered would indicate convective regions within ice clouds during aircraft collocation, an optimal scenario to identify CCs for this research.

Figures 6 and 7 show the remote sensing and in-situ data visualizations. Considering all flights during IMPACTS 2020, the time period around 08:00:00PM UTC 25 Jan 2020 was the time when the ER-2 and the P-3 aircraft were most precisely collocated, with a minimum horizontal separation of ~250 m at the center point of the collocated leg. Figure 6 shows a 2-

dimensional view of the radar reflectivity data from the CRS, and IWC and mean number diameter (MND) derived from the 2DS and HVPS-3 at a height of 6 km above ground, and a temperature of -19 °C. Figure 7 shows a 2-D view of the Doppler velocity measured by the CRS aboard the ER-2, and the vertical velocity and temperature measured by the TAMMS probe aboard the P-3. In both figures, the collocated area where the two aircraft can be assumed to be measuring roughly the same cloud segment, and therefore the same region of convection, is highlighted. The altitude of the P-3 is superimposed on the CRS visualizations for reference. It is seen that in areas of cloud with enhanced reflectivity and upward motion measured by the CRS, the vertical velocity and temperature measured by the TAMMS enter a state of perturbation and rapid variation, with increases (decreases) in temperature coinciding with increases (decreases) in positive vertical air motion from 08:04:15PM to 08:04:45PM UTC. Enhanced reflectivity and Doppler velocity measured by the CRS can also be visually associated, during the same time period, with an increase in IWC and MND as measured by the particle probes aboard the P-3. Three separate radar confirmed CCs were later identified, as described in Chapter 3b, that coincide with the remote sensing radar measurements during the collocated time period in Figures 6 and 7. The increases in IWC and MND during convection are consistent with similar increases observed in cloud-top GCs (Plummer et al. 2014, 2015), and in elevated CCs (Rauber et al. 2014). The increases in temperature associated with positive vertical motion is interesting, as this behavior is theorized to exist within GCs as they release latent heat from the deposition of water vapor onto ice particles (AMS 2022), which is consistent with the idea that GCs are self-sustained by the preservation of positive vertical motion though thermodynamically initiated convection (Ludlam 1956), or as warm air rises from lower altitudes.

ii. Statistical analysis visualization

A visualization of the statistical relationship between vertical motion measured by the TAMMS and particle size distributions derived from the particle probes is shown in Figure 8. The 2-dimensional histogram is overlayed with the MMD and MND, as well as the number of samples used to calculate the values in each vertical velocity bin. This statistical representation is based on bulk parameters, only filtering out missing data, or data between flight legs. It is meant to give a general and comprehensive representation of how the bulk microphysical properties of clouds change as a function of vertical velocity. The number of samples collected decreases logarithmically as vertical velocity increases in either the positive or negative direction because the bulk of the measurements were acquired in stratiform cloud. The MMD of particles was always higher than the MND because particle size is weighted by mass in its calculation (Leroy et al. 2016). Overall, the most noticeable feature of Figure 8 is that there was a higher concentration of particles with 0.1 mm < D < 1 mm for the largest vertical velocities, with the largest increase for maximum dimensions between 3 mm and 4 mm.

The same data used in Figure 8 is used to produce the normalized histograms in Figures 9 and 10. These figures show how the frequency of distributions of microphysical properties vary according to whether they were observed in updrafts, downdrafts, or stratiform regions. The subplots are differentiated by temperature, either above or below 0 °C, and by the instruments used to determine the microphysical properties in either the combined HVPS/2DS product or the FCDP measurements. Figures 9 and 10 show the frequency distributions of bulk water content and MND, respectively. Figure 9 shows that the data with IWC derived from the HVPS/2DS for temperatures > 0 °C, and the LWC data derived from the FCDP for temperatures less than 0° C is sparse. This makes physical sense because even though there will be liquid and ice particles

present in mixed phase clouds above and below freezing, liquid particles may be less representative in environments where they are actively freezing. Each histogram is color coded to represent samples of data where the TAMMS measured convective as well as stratiform regions; labelled downdrafts, updrafts, and stratiform regions, respectively. Stratiform regions are assumed to have vertical motions between -1.5 ms^{-1} and 1.5 ms^{-1}. This threshold was determined based on the common convention of -1 $ms^{-1} < W < 1$ ms^{-1} to identify stratiform regions, which showed nearly identical results, but sensitivity analysis determined -1.5 $ms^{-1} < W < 1.5$ ms^{-1} better represented the shape of the data. Figure 9 showed a bi-modal distribution of IWC values for both updraft and downdraft regions with temperatures below 0 °C. A larger proportion of data within updrafts contained around 0.5 g m^{-3} of IWC than data within downdrafts, while downdrafts showed a higher concentration of data around 0.2 g m^{-3}. However, both updrafts and downdrafts showed an increased concentration of IWC values around 1.75 g m^{-3}. This is consistent with the findings of Plummer et al. (2014, 2015) who showed an increase in IWC within GCs, which were possibly measured along with CCs during IMPACTS. The normalized histograms representing MND as measured by the 2DS and HVPS in Figure 10 similarly show a bi-modal distribution for 'updraft' and 'downdraft' regions. There is a mode centered around 4 mm for both updrafts and downdrafts, which suggests that particle sizes are larger for periods where increases in negative or positive vertical velocity are present. Figures 9 and 10 are consistent with trends observed in GCs. Because there was not collocation between the ER-2 and P-3 for most of the flight time, it was difficult to unambiguously determine the cloud-top height data necessary for identifying GCs. Therefore, a set of criteria was developed for identifying cores of elevated CCs, which are not restricted in definition to cloud-top regions.

b. Collocated case study

i. Radar confirmed CCs

Several algorithms were developed to identify the location of CC cores through remote sensing data from the CRS. Because the temporal resolution of the radar data was 1-s after post processing, any instance of a CC core became the center point of a radar-confirmed CC that was to be 5 seconds in duration. The ER-2, which housed the CRS instrument, has a typical flight speed of 210 ms^{-1}, so 5 seconds of flight time corresponds to ~1 km of horizontal distance. This timeframe was chosen to be consistent with previous studies that have used similar methods to identify the presence of cores of cellular convection (Kumjian et al. 2014).

First, an algorithm (alg1) that uses the relative local dB values of radar reflectivity was used to identify CCs under the assumption that both CCs and GCs are characterized by a local maximum in dBZe values. From each instance of time that indicated a CC core, the previous and subsequent two points in time were considered to be within CC. This algorithm identified the most CC regions when applied to the overall dataset, due to having the most relaxed criteria.

A second algorithm (alg2) used the same reflectivity criteria as alg1 but filtered out potential CC cores by examining Doppler radar velocity measured by the CRS. The inclusion of Doppler radar velocity measurements to identify CCs follows the usage of vertical velocity information to define GC regions in Wang et al. (2020), which is based on the fact that CCs typically harbor large positive vertical velocity values at their centers (Rosenow et al. 2014). Any point in time that did not correspond to a radar velocity placement of at least the 25^{th} percentile was not considered to be a CC core. Radar velocity measurements, however, define the vertical motion of particles, and not the vertical velocity of the air. Consequently, the radial velocity of particles measured include a contribution from the fall speeds of particles, which increases the

downward component of the velocity vectors relative to the TAMMS data. Because alg1 over-identified regions containing CCs due to its loose criteria using only reflectivity, alg2 was considered more sophisticated because it also incorporates the dynamical properties of the cloud segments being analyzed.

Finally, a third algorithm (alg3) used the same reflectivity criteria as alg1 and alg2 but estimated the vertical motion of the atmosphere differently. Instances of local maxima of dBZe were identified to be potential CC cores or not by using a radar estimated vertical air motion calculation that considered the reflectivity-weighted terminal fall velocities of the cloud particles (Heymsfield et al. 2018; Kalesse et al. 2013; Su et al. 2009). Because the CRS records data at nadir, the particle motion was considered to be entirely vertical, so that combining the Doppler velocity with the estimated fall velocities of the particles gave an estimate of vertical air motion. This algorithm is less restrictive than alg2 but more restrictive than alg1 at identifying CC cores.

The CC regions identified by all three algorithms (alg1, alg2, alg3), on the flight days of January 25th, February 1st, and February 5th, 2020, during periods of aircraft collocation, where both TAMMS data and remote sensing data from the CRS were available, were compared against the TAMMS data. Of the segments analyzed, all were considered in the analysis, but only the case from January 25th between 08:04:40 and 08:05:20 PM UTC is presented here. Figure 11 compares Doppler radar velocity, radar estimated vertical velocity, and dBZe measurements at a range gate from the radar that coincides with the altitude of the P-3 aircraft. The CRS and the TAMMS instruments were assumed to be measuring the same population of cloud particles due to the collocation of the two aircraft. Figure 11a shows the dBZe and radar estimated vertical velocity with the points identified as local dB maxima indicated. Datapoints whose measurements fall below the 25th percentile of radar estimated vertical velocity measurements

for the entire flight segment are also indicated. Alg3 was applied to these data so that any point identified as a local maximum and a radar estimated vertical velocity above the 25th percentile was considered to be a CC center point (core).

Based on the criteria discussed above for identifying radar confirmed CCs using alg3, there are four such cells identified in Figure 11. Three of the CCs were 5 seconds, or ~1km, wide, while one CC contained two cores, spanning over 8 seconds, or ~1.7km. CCs with multiple cores were treated as one wider CC. These regions were compared to the TAMMS air velocity data, shown in Figure 11d. The TAMMS vertical velocity measurements exhibited behavior within the radar-identified CC consistent with previous observations within CCs. For data collected within CCs, there were considerable fluctuations in TAMMS vertical velocity, and the center-point of the fluctuations resided right around 0 ms^{-1}.

ii. TAMMS criteria for CCs

Based on the case study in Figure 11, and the two other time periods where radar confirmed CCs and data from the TAMMS probe were present, a statistical analysis was performed to determine patterns in the TAMMS vertical velocity data within and between CCs.

Considering the 2020 January 25th 08:04:29 to 08:05:12, February 1st 01:12:03 to 01:12:27, and February 5th 09:57:09 to 09:57:52 PM UTC time periods, the following TAMMS vertical velocity characteristics were consistent across all periods within CCs *identified by alg1*: The range of TAMMS vertical velocity values in each CC region was greater than 0.4 ms^{-1}, the range of percentiles of values, considering the collocated data segment in question, was greater than 7, and the largest vertical velocity was higher than the 15th percentile. The following characteristics were consistent across all CC regions *identified by alg2*: The range of TAMMS vertical velocity values was greater than 1.7 ms^{-1}, the range of percentiles of values considering

the collocation segment in question was greater than 16, and the largest vertical velocity was higher than the 29th percentile. And the following characteristics were consistent for every CC region *identified by alg3*: The range of TAMMS vertical velocity values was greater than 1.2 ms^{-1}, the range of percentiles of values considering the collocation segment in question was greater than 16, and the largest vertical velocity was higher than the 30th percentile.

The implication is that CCs can be adequately identified, without the need for remote sensing measurements, by using the TAMMS air motion characteristics discovered within CCs as discussed above. It is necessary to consider that, when comparing the radar estimated vertical air motion to the vertical air motion recorded by the TAMMS, the location of the measurements at the same time is not identical because of the horizontal separation between the aircraft. Therefore, considering the range of TAMMS vertical velocities as opposed to exclusively looking at the absolute vertical velocities of individual points with substantial vertical motion is important. Thus, the TAMMS characteristics for radar confirmed CCs include both a range of velocities, and a relative peak in those velocities. The behavior of the data measured by the TAMMS within CC regions identified by alg3 was used to develop an algorithm for identifying CCs using only in-situ velocity data that targets banded structures and cellular convection within snowstorms. Alg3 was used to identify CCs with the TAMMS due to the overly lenient criteria associated with alg1, and because alg2 did not consider some substantially high reflectivity measurements a CC core due to the lack positive particle radial velocity measurements.

c. In-situ characteristics of CCs using only P-3 instruments

i. Defining cloud penetrations

The algorithm that considers the air motion characteristics recorded by the TAMMS during collocated radar confirmed CC regions described in Chapter 3bii was applied to the larger

statistical dataset for all in-situ observations from every P-3 flight during IMPACTS 2020. Using this algorithm is a novel approach to defining regions of convection as past studies have simply used positive vertical velocity measurements alone as a definition. Namely, by training the TAMMS algorithm to detect vertical velocity characteristics that match those found in isolated regions of elevated cellular convection accompanied by locally enhanced reflectivity during the collocated case study analysis, CCs detected during statistical analysis by the algorithm utilizing only TAMMS data could be treated as similarly isolated regions of cellular elevated convection, targeting banded regions. The dataset was first divided into segments that were appropriate for calculating the percentile of each vertical velocity measurement; these segments of time are referred to as "cloud penetrations." For any 20-second span of time when TAMMS velocity data were available, at least one of the first 7 points, the middle 6 points, and the last 7 points of data had to contain at least one instance of cloud particle detection (for a total of 3 points). When this criteria was first met, this was considered the first instance of cloud penetration. After a cloud penetration was detected, the first datapoint to not meet this criteria was considered the end of the cloud penetration. Lastly, any cloud penetration segment that did not contain at least 12 1-second time periods when cloud particles were recorded was removed from the dataset of cloud penetrations.

ii. TAMMS confirmed CCs and their characteristics.

Using the criteria described in 3bii, CC regions were identified and labeled for each cloud penetration. Overall, there were 94 cloud penetrations, of which 29 contained TAMMS confirmed CCs. Additionally, of the 29 cloud penetrations that contained at least one CC, 878 CCs were identified. A statistical dataset that included coincident IWC, LWC, total number concentration, particle size distribution, temperature, dewpoint, and SLW presence was

generated and analyzed. The dataset was separated into time periods within and between CCs. There were 117,985 datapoints considered to be between CCs, and 6,582 datapoints within CCs.

Averaged MMD measurements were marginally larger within CCs than between, but averaged MND was 0.3 mm larger between CCs than within. This increase in MND between CCs reduces the likelihood that the CCs being recorded were GCs, as studies such as Plummer et al. (2014, 2015) showed an increase in particle maximum dimension within GCs. This also conflicts with analysis presented in Chapter 3ai, where more intense vertical velocity measurements were associated with a higher concentration of larger particles. Before considering the inaccuracies associated with the methods used to detect CC regions, the observed trends are consistent with certain regions of cloud penetration between CCs being situated in residual stratiform precipitation fall streaks below active GCs, in which case larger falling particles ejected out of the bottom of a GC are measured.

Distributions of IWC were similar within and between CCs, which implies that although the wide area of convection associated with CCs is capable of supporting larger particles (Rauber et al. 2014), the mass of ice particles present was similar to that recorded in the stratiform regions between CCs. However, LWC was found in quantities 2.3 larger within CCs than between CCs, and total number concentration averaged 2.8 times larger within CCs compared to between. These findings suggest that larger quantities of small liquid cloud particles exist within CCs compared to between CCs, and that riming may not be an important growth mechanism within TAMMS confirmed CCs considering their unremarkable IWC quantities.

Temperature measurements were 2.4 °C higher within CCs than between, and dewpoint depressions were 0.8°C smaller within CCs than between, indicating a slightly warmer but also more humid environment within CCs. Thermodynamically, elevated temperatures are indicative

of heat being generated by latent heat release supplying the convection present within CCs. Additionally, if a significant number of were GCs included in the CC population, an increase in temperature could be explained by the release of latent heat associated with ice particle growth. SLW was present 24.6% of the time within CCs, while all CCs measured contained at least one instance of SLW. This finding coincides with Rauber et al. (2014) which also observed SLW presence within regions of elevated convection in winter storms.

4. Conclusions

The analysis presented here to contrast the properties inside and between CCs differs from previous studies that used remote sensing data only to identify the presence of elevated convection or cloud-top GCs in that only in-situ measurements of vertical velocity were used to identify CCs. Because there were only 0.35 hours of data when the ER-2 and P-3 were separated by less than 1.4 km during IMPACTS in 2020, this study developed a scheme to identify CCs only using data from the precise in-situ air motion measurements from the TAMMS probe aboard the P-3. This was done by training the scheme using radar-identified CCs for the few time periods the P-3 and ER-2 were deemed to be collocated. The small-scale air motion associated with TAMMS confirmed CCs was variable, meaning the ranges of velocities were relevant in defining CCs. But, while there was variability in the vertical velocity measurements in CCs, a component of the positive vertical motion was also identified. Specifically, using the algorithm described in Chapter 3bii to identify CC regions for in-situ analysis, the measurements of the TAMMS within CCs showed ranges of vertical velocity of 1.2 ms^{-1}, percentile ranges of 16 percent, and local maximum vertical velocity of at least the 30^{th} percentile. Using CCs identified

by the air motion data, the microphysical and thermodynamic properties derived from the in-situ cloud and thermodynamics probes were contrasted inside and outside CCs.

a. Results

Averaged measurements of ice water content (IWC) and median mass diameter (MMD) derived from the cloud probe data within (between) CCs were similar, with means of 0.35 g m^{-3} and 1.72 mm (0.36 g m^{-3} and 1.64 mm) for IWC and MMD respectively. This indicates that, assuming CCs were primarily sampled as opposed to GCs, even though CCs may have the potential to support ice particle growth through sustained suspension by convection, they lacked the protective environment that would allow for enhanced growth during IMPACTS. Alternatively, turbulence could have thoroughly mixed the ice inside and outside the CCs, or the stratiform regions between CCs could have supported the continued growth of ice even if they did not support the growth of liquid.

The derived median number diameter (MND) was on average 0.3 mm larger between CCs than within CCs, which is inconsistent with previous measurements in updrafts in winter storms. Thus, it may be more likely that the trends observed here are associated with shear that could cause the particles growing in the updrafts to fall adjacent to those updrafts, or due to the lack of good collocation between aircraft affecting the quality of the algorithm used to identify CCs. However, another explanation could be that the CCs identified by the TAMMS were located adjacent to the fall streaks of large particles being ejected out of the bottom of cloud-top GCs.

LWC was found in quantities 2.3 larger within CCs than between, with quantities averaging 0.23 g m^{-3} within CCs and 0.11 g m^{-3} between CCs. Total number concentration (N_t) averaged 2.8 times larger within CCs compared to between, with an average of 3.7 x 10^4 m^{-3} within CCs and 1.3 x 10^4 m^{-3} between CCs. These LWC and N_t measurements, illustrated in Figure 12b and

12d, are consistent with Plummer et al. (2014) and Rauber et al. (2014) who suggest that CCs provide an environment that allows for falling particles to undergo riming and aggregation as they fall through cloud particles, and Brechner et al. (2023), who found numerous small particles in updrafts for oceanic tropical clouds, which they attributed to larger supersaturations and possible secondary ice crystal production mechanisms.

Temperatures were on average 2.4 °C larger within CCs than adjacent to CCs, potentially due to the release of latent heat as ice crystals grow, or due to the advection of warmer air from lower altitudes. Dewpoint depressions were on average 0.8 °C smaller within GCs, likely due to the rapid rise of more saturated air through the unsaturated environments associated with elevated convection (Murphy et al. 2017). SLW was found within all GC regions identified by the TAMMS, consistent with previous studies showing the prevalence of SLW in both GCs and CCs. There was a 9% decrease in SLW presence between generating cells compared to within.

b. Potential inaccuracies

Diagnosing the vertical nature of air motion through remote sensing is difficult because Doppler velocities measure the sum of the air motion and the particle fall speeds. Given the large variability in ice crystal fall velocities, the use of a relationship between radar reflectivity and reflectivity-weighted fall speeds has considerable uncertainty; the CRS measures the sum of the vertical component of particle motion directly due to the radar beam being nadir, which helped to improve upon those inaccuracies due to the vertical nature of the fall velocities being corrected for. Ice particle fall velocities vary as a function of particle shape, size, and mass, as well as the altitude of the particle due to the atmosphere being denser at lower altitudes and producing more drag on the particles as they fall, although there are simple and accurate methods for adjusting fall velocities for altitude. Thus, while radar estimated vertical velocities from prior

observational studies were used to derive the air motion for defining CC cores in this study, the applicability of this relationship for the IMPACTS measurements is unknown. Therefore, a future study should derive a reflectivity-fall speed relation specific for IMPACTS by using the temperature-dependent measured size, shape, and phase distributions during IMPACTS to directly compute the radar and fall velocity of each particle.

The definition of a CC identified by diagnosing in-situ vertical velocity measurements within radar confirmed CC regions does not have much precedent. The exact qualities to be looking for were not known prior to the initiation of this research. Given that the ER-2 and P-3 were deemed to be aligned when they were horizontally separated by 1.4 km there is a good chance that misalignments of the ER-2 and P-3 could have complicated the identification of CCs. However, a finer criterion for alignment could not be used because that would have prevented sufficient data points being available for the analysis. That is to say, CC regions identified by the TAMMS may not have been identified during a more established type of analysis such as an analysis that primarily utilized remote sensing.

c. Future studies

More case studies of valid horizontal coordination between the P-3 and ER-2 aircraft with valid TAMMS data would have allowed for a more statistically significant representation of how the small-scale air motion behaved within regions of radar confirmed CCs. Given more datapoints of coincidental in-situ air motion and remote sensing measurements, there could be an opportunity for diagnosing TAMMS air motion data with respect to radar confirmed CCs in a more complete way. An algorithm for identifying TAMMS confirmed CCs could also be generated and then applied to time segments of collocation that were not used in its development for the purpose of using remote sensing to verify the existence of CCs found by the TAMMS,

enhancing confidence in the accuracy of such an algorithm. Such data does exist from the 2023 phase of the IMPACTS campaign, where numerous instances of collocation between aircraft with simultaneous remote sensing and in-situ measurements are available. A derived cloud-top height product from the WSR-88D Weather Surveillance Doppler Radar network could be instrumental in classifying TAMMS-confirmed CCs by depth below cloud top. This would enable the approximate separation of GCs from CC measurements, allowing for further diagnosis and reasoning behind their microphysical characteristics.

Figures and Tables

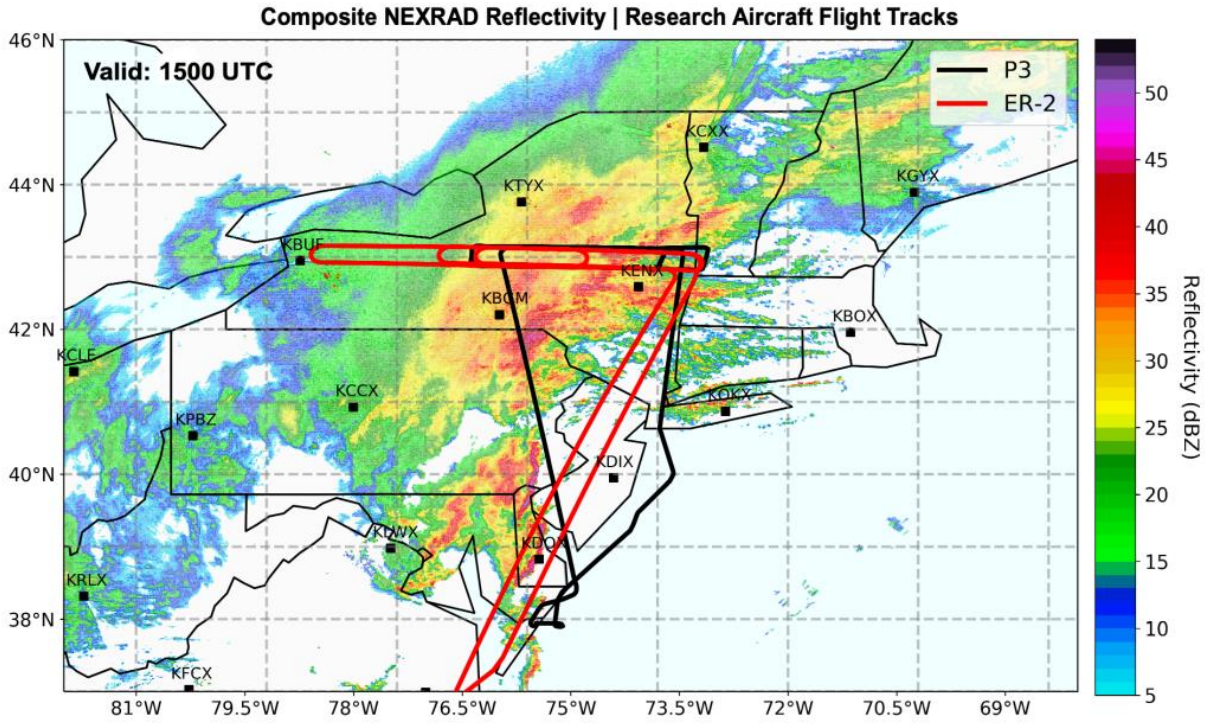

Figure 1: P3 (black) and ER-2 (red) flight tracks for 7 February 2020. WSR-88D composite reflectivity valid 1500 UTC 7 February (Reprinted from Varcie et al. (2021)).

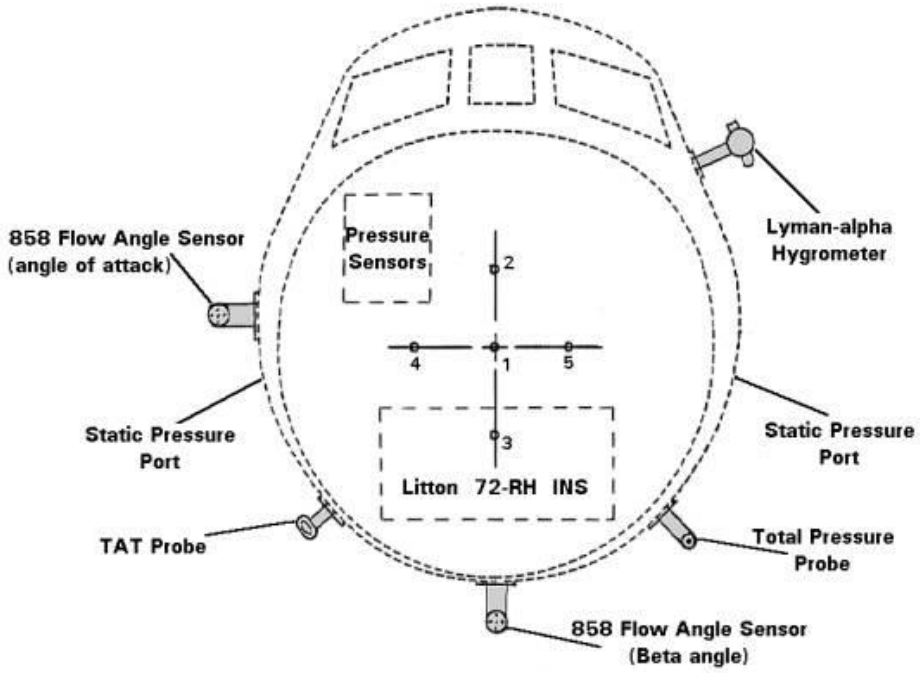

Figure 2: Flush P-3B Radome Pressure System.

https://www.gte.larc.nasa.gov/pem/considine.htm

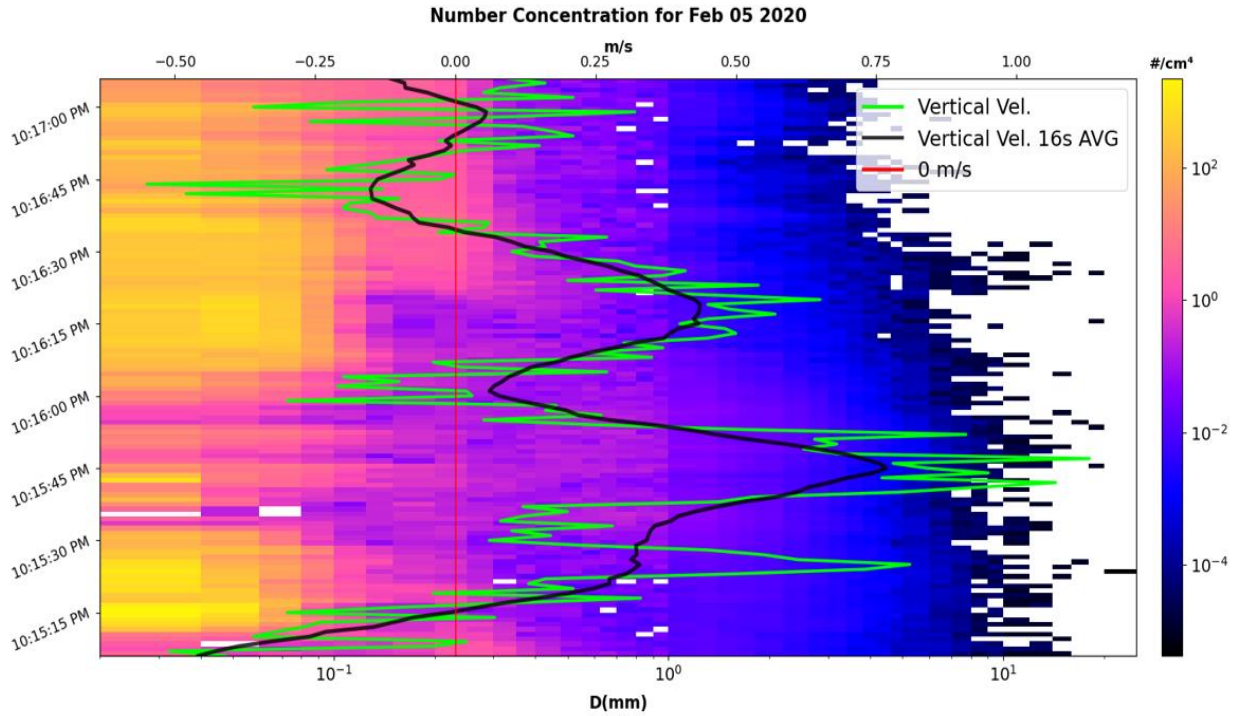

Figure 3: In-situ particle size distribution derived from the 2DS and HVPS-3 with TAMMS vertical velocity superimposed as both a 1-second and 16-second rolling average (green and black lines respectively), and a 0-line for vertical velocity in red. Valid from 10:15:10 to 10:17:03 PM GMT on the flight day of February 5th, 2020.

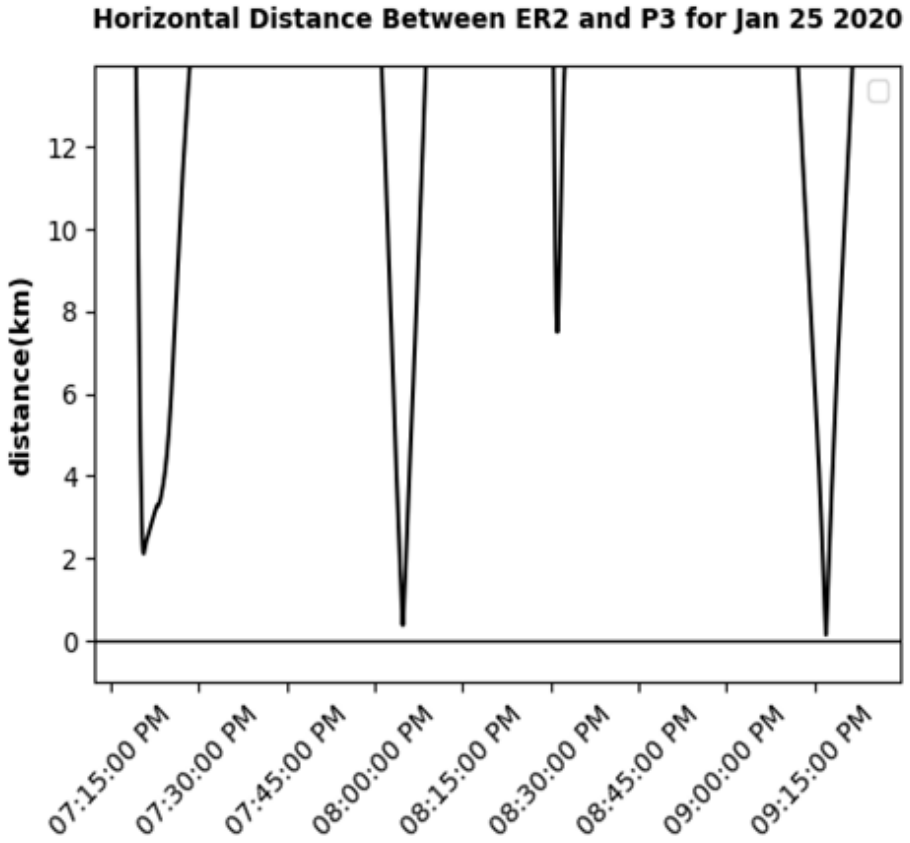

Figure 4: Horizontal distance between the P-3 and ER2 aircraft using a great circle calculation as a function of time for the January 25th, 2020, flight day.

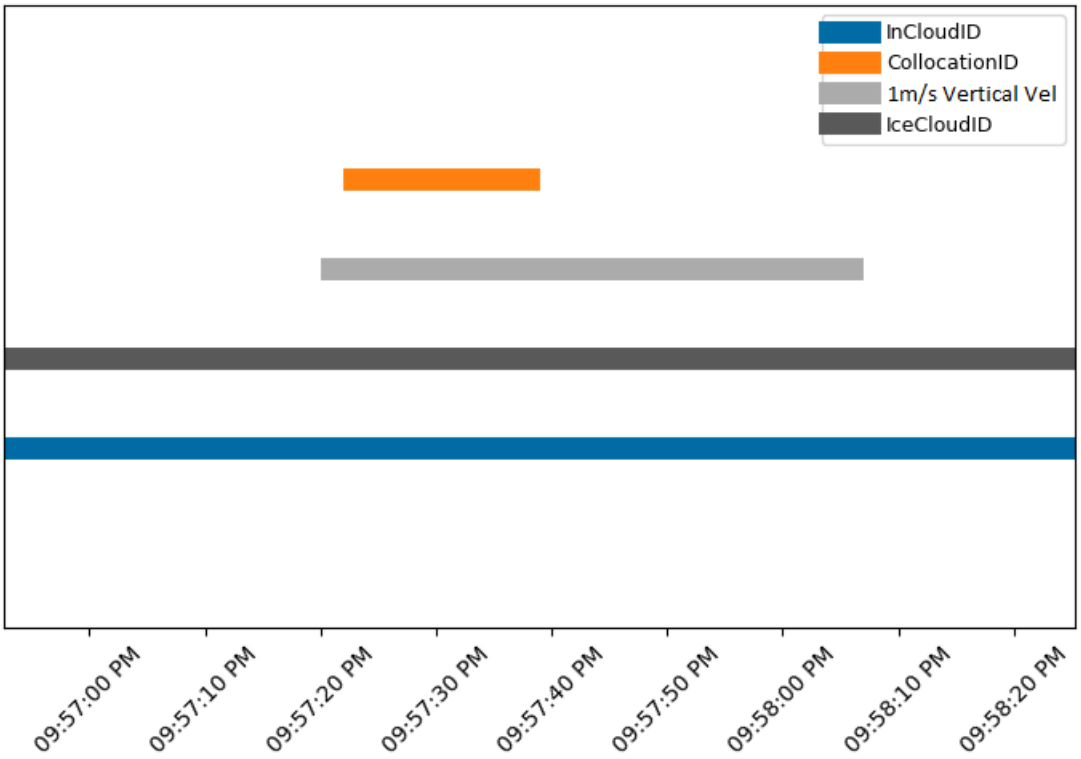

Figure 5: Various IDs represented on a time series from 09:56:55 to 09:58:25PM for the February 5th, 2020, flight day.

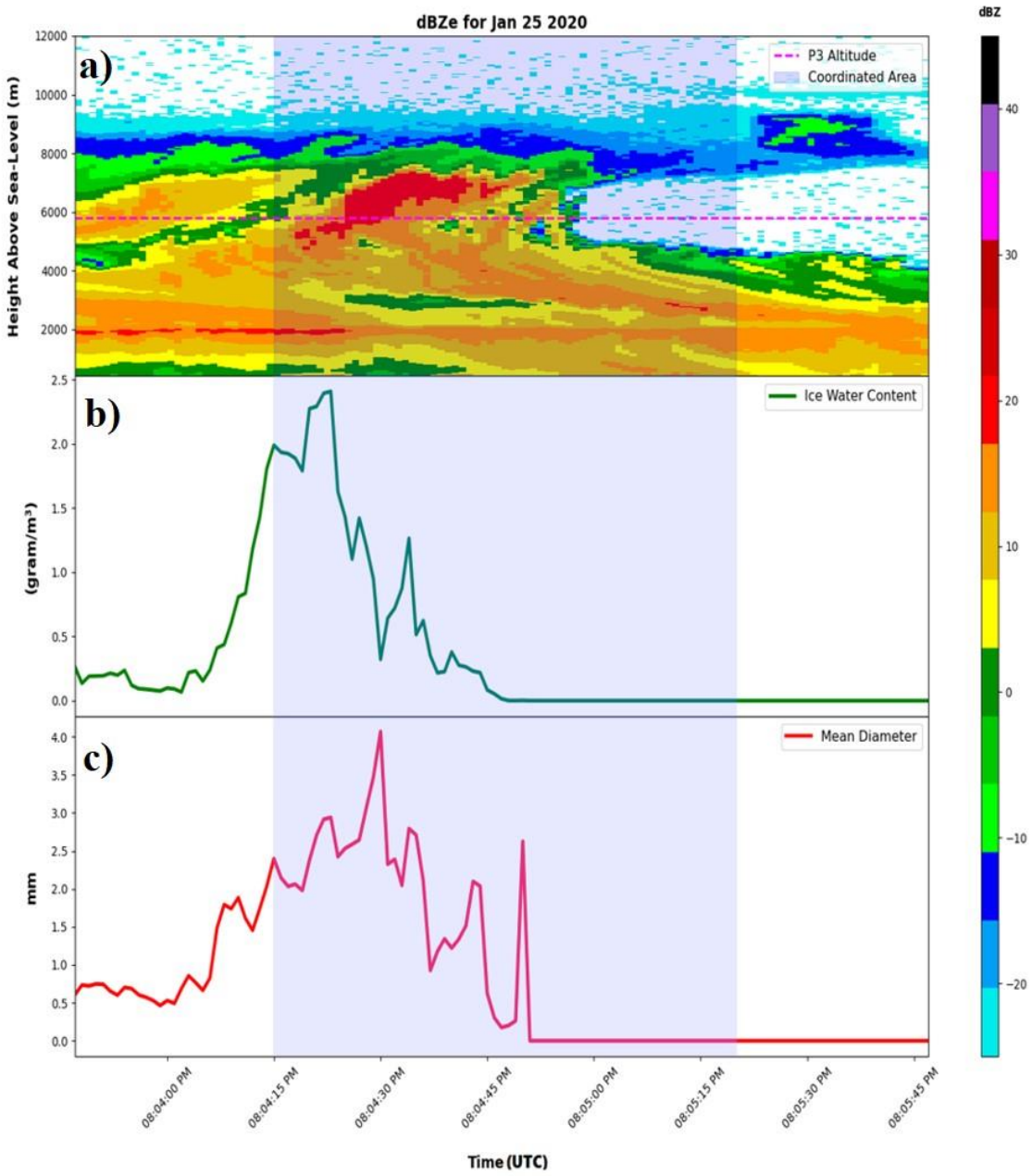

Figure 6: a) dBZe measurements from the ER-2 CRS with superimposed P-3 altitude (dotted pink) and a highlighted region for aircraft collocation (light blue). b) IWC derived from the 2DS and HVPS size distributions (green) with a highlighted region for aircraft collocation (light blue). c) Mean number diameter (red) with a highlighted region for aircraft collocation (light blue). Valid from 08:03:46 to 8:05:46PM on the flight day of January 25th, 2020.

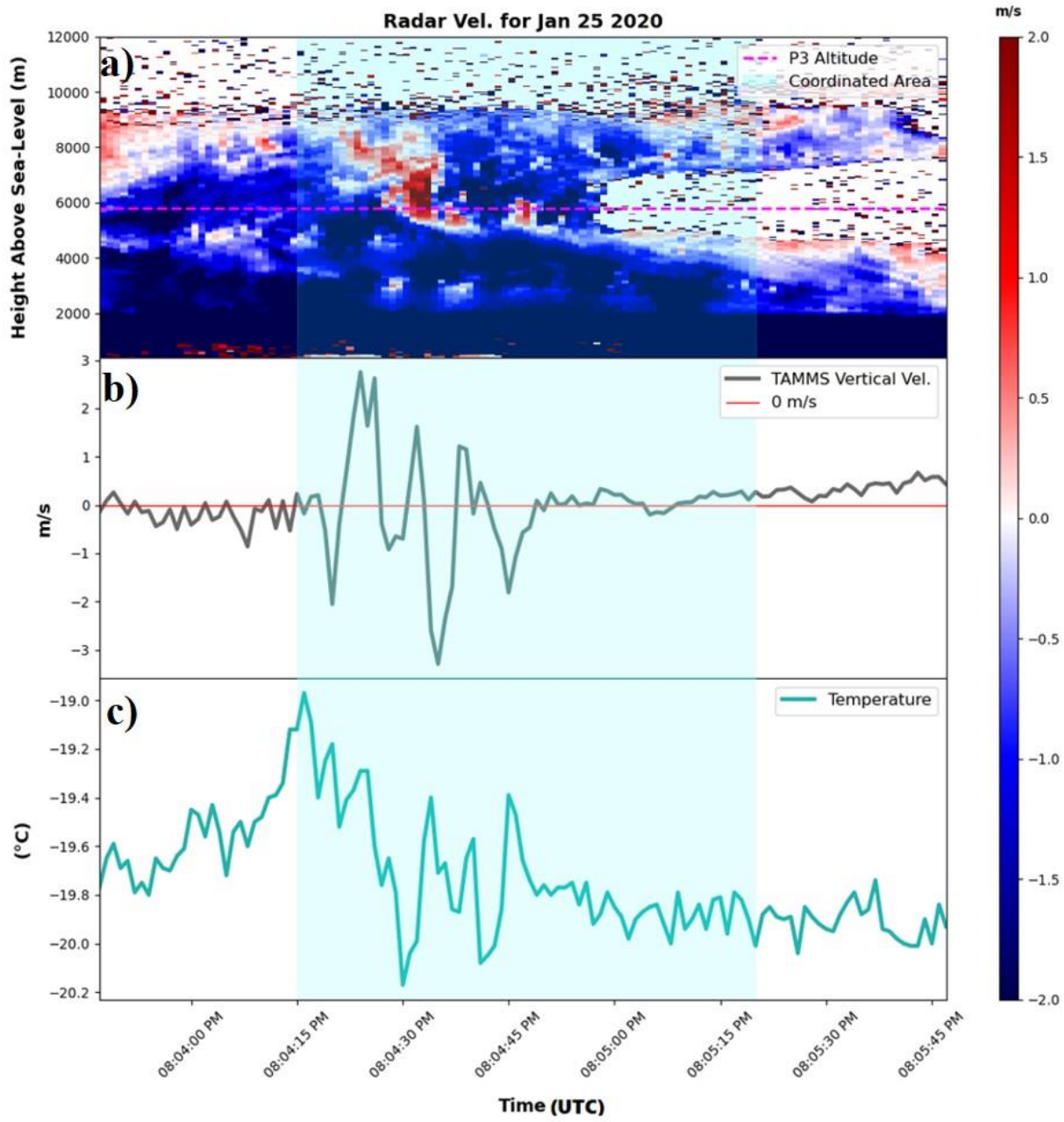

Figure 7: a) Radar Doppler velocity measurements from the ER-2 CRS with superimposed P-3 altitude (dotted pink) and a highlighted region for aircraft collocation (light blue). b) TAMMS vertical velocity (gray) with a highlighted region for aircraft collocation (light blue). c) Temperature (teal) with a highlighted region for aircraft collocation (light blue). Valid from 08:03:46 to 8:05:46PM on the flight day of January 25th, 2020.

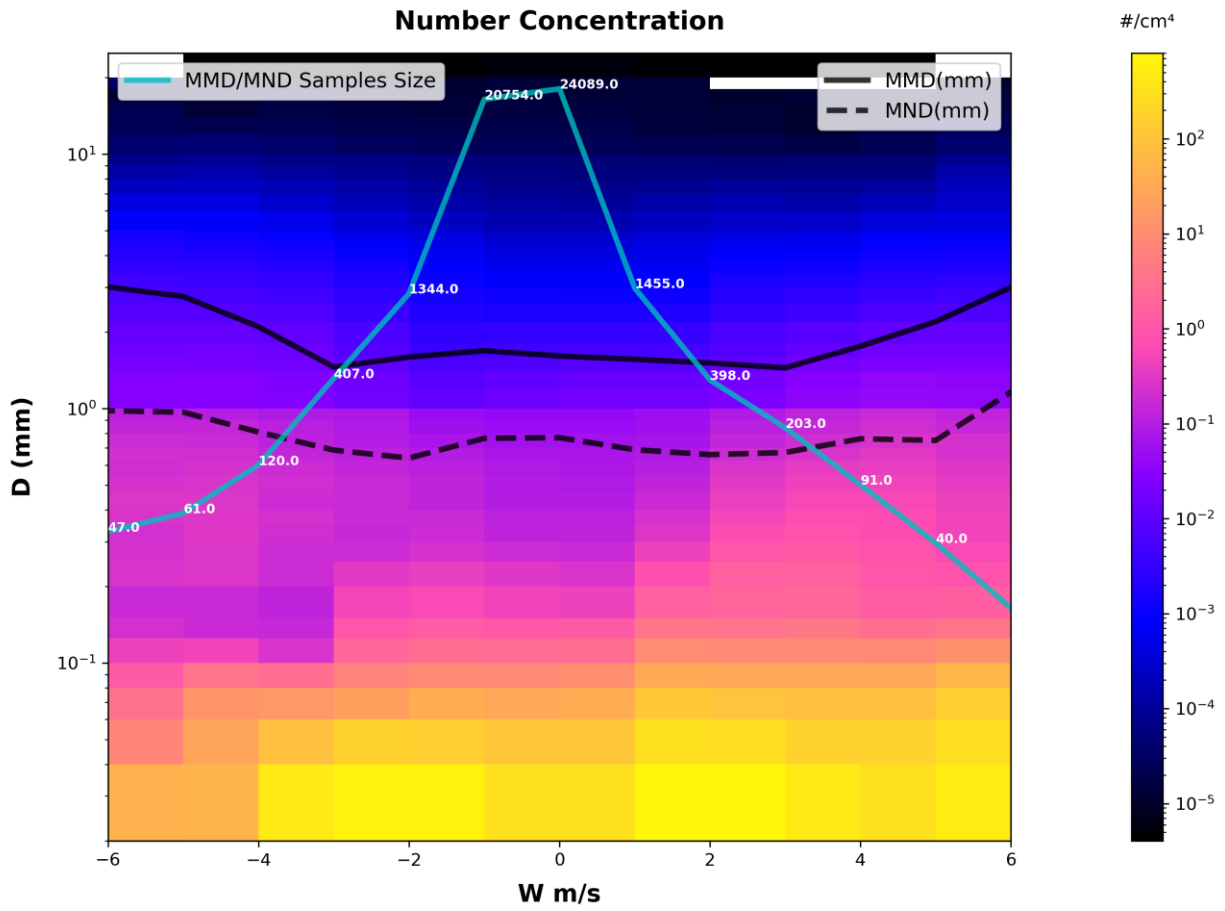

Figure 8: Average number distribution function measured by the 2DS and HVPS plotted as color contours as derived for different vertical velocity ranges as measured by the TAMMS. Median mass and mean dimensions superimposed (solid and dashed black lines respectively). Number of samples used in producing MMD and MND line-plots represented by the teal line-plot.

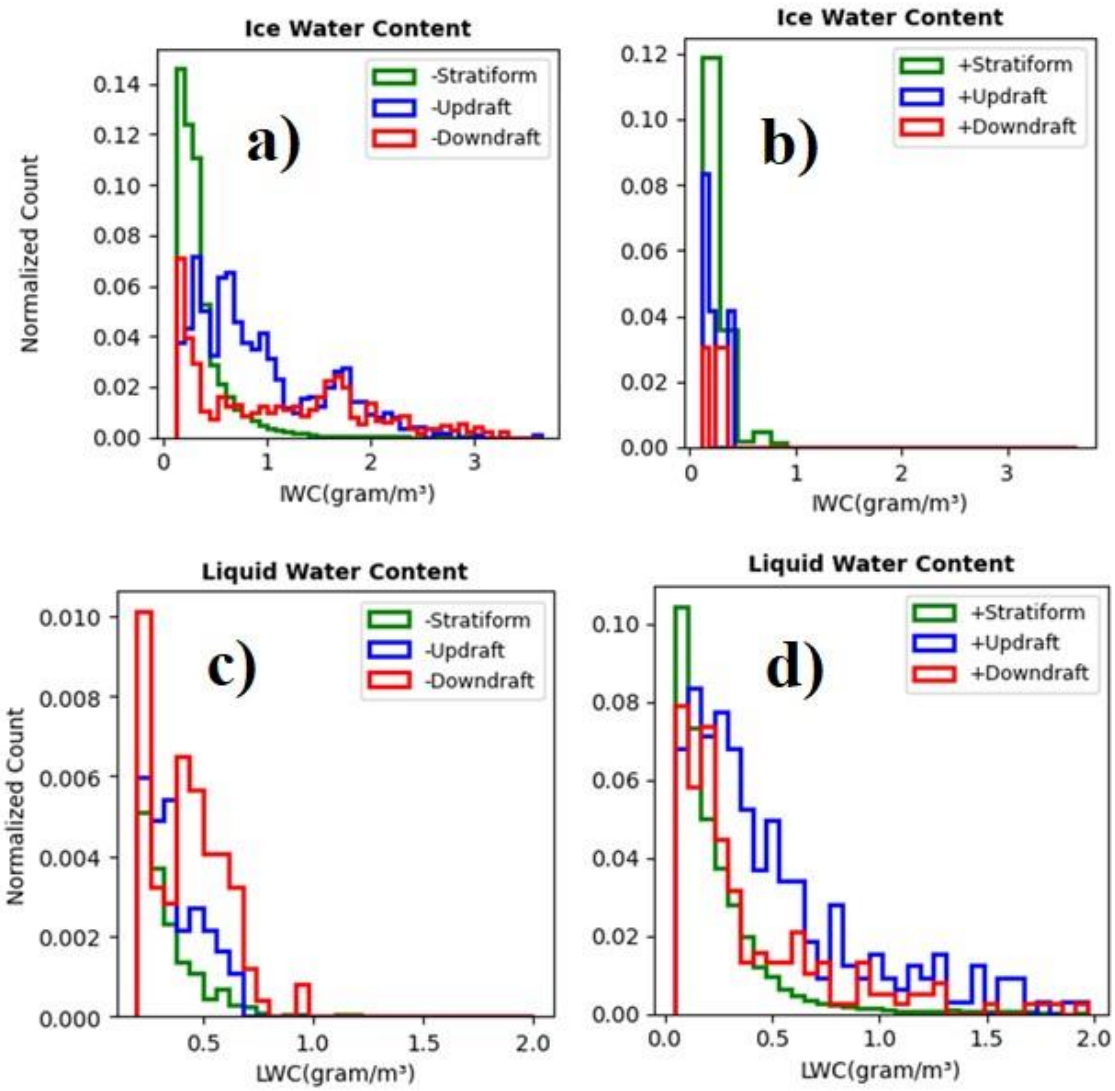

Figure 9: Normalized distribution function of 2DS+HVPS ice water content (a and b) and FCDP liquid water content (c and d). Temperature less than 0°C (a and c) and greater than 0°C (b and d). Data differentiated by TAMMS vertical velocity measurements; where updraft ($W > 1.5ms^{-1}$), downdraft ($W < -1.5ms^{-1}$), and stratiform ($1.5ms^{-1} > W > -1.5ms^{-1}$) are represented by the blue, red, and green lines respectively.

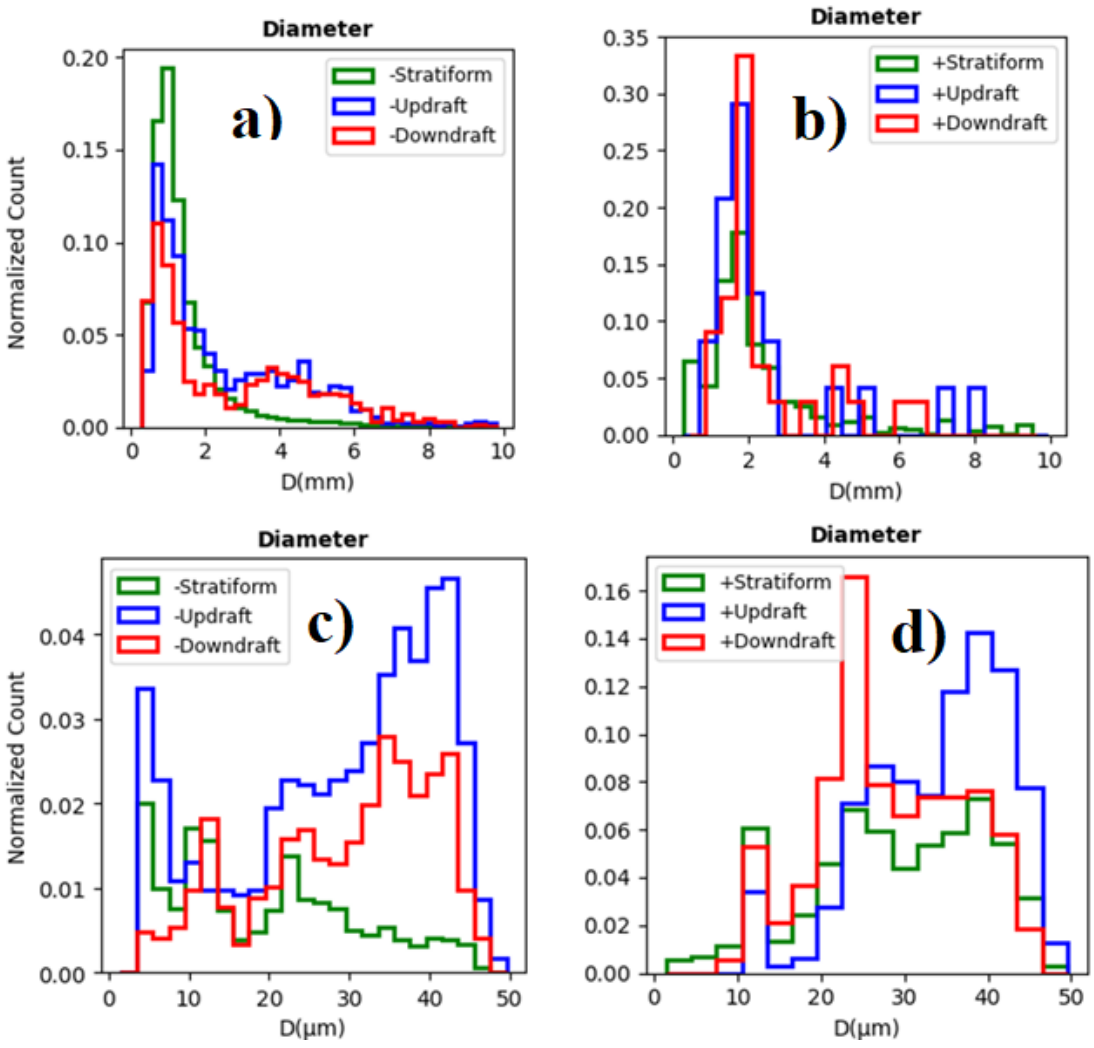

Figure 10: Normalized distribution function of 2DS+HVPS particle diameter (a and b) and FCDP particle diameter (c and d). Temperature less than 0°C (a and c) and greater than 0°C (b and d). Data differentiated by TAMMS vertical velocity measurements; where updraft ($W > 1.5ms^{-1}$), downdraft ($W < -1.5ms^{-1}$), and stratiform ($1.5ms^{-1} > W > -1.5ms^{-1}$) are represented by the blue, red, and green lines respectively.

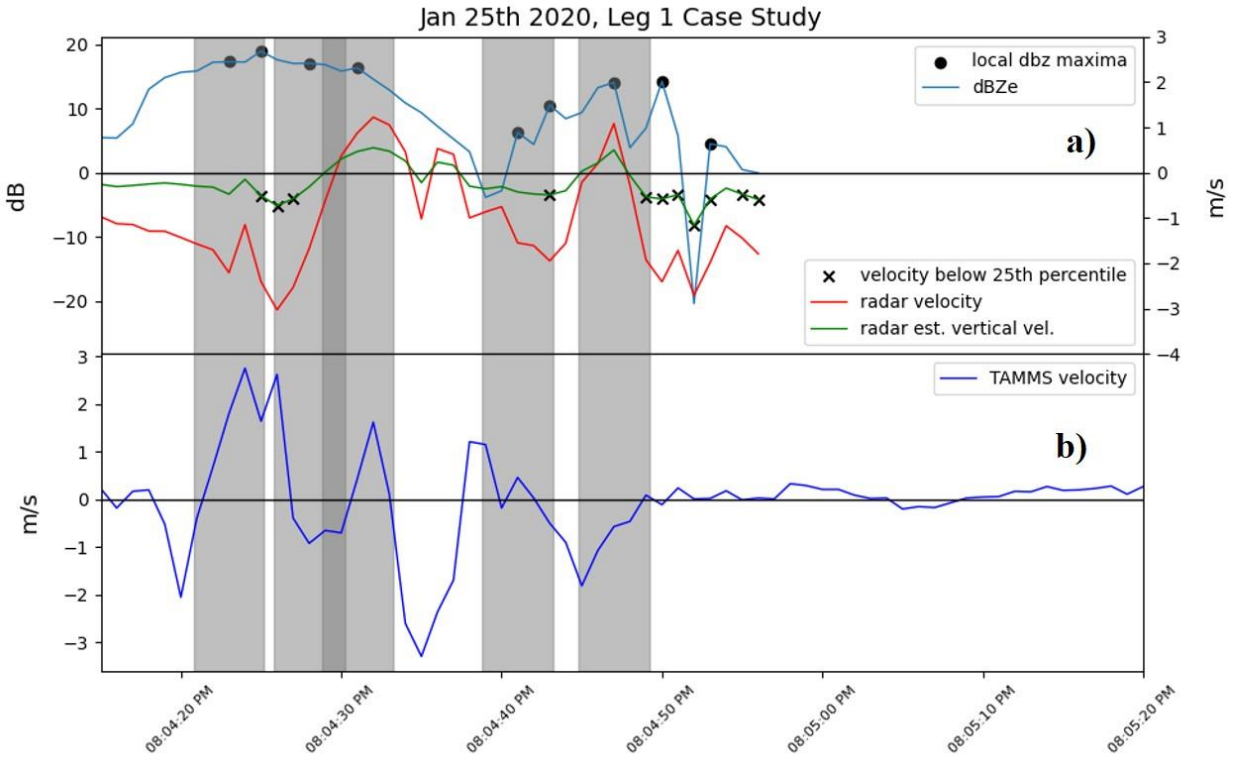

Figure 11: a) Radar Doppler velocity from CRS on ER-2 and b) estimated vertical air motion from the range gate corresponding to P-3 location (red line and green lines, respectively), with X markers indicating values below the 25th percentile for the leg (black). Radar reflectivity measured from the range gate respective to the P-3 location (light blue line), with circle markers for points of local maxima (black). TAMMS vertical velocity measurements on the bottom subplot (royal blue line), with both subplots featuring shaded regions marking the presence of radar confirmed CCs (gray). Valid for the period of aircraft collocation from 08:04:15 to 8:05:20PM on the flight day of January 25th, 2020.

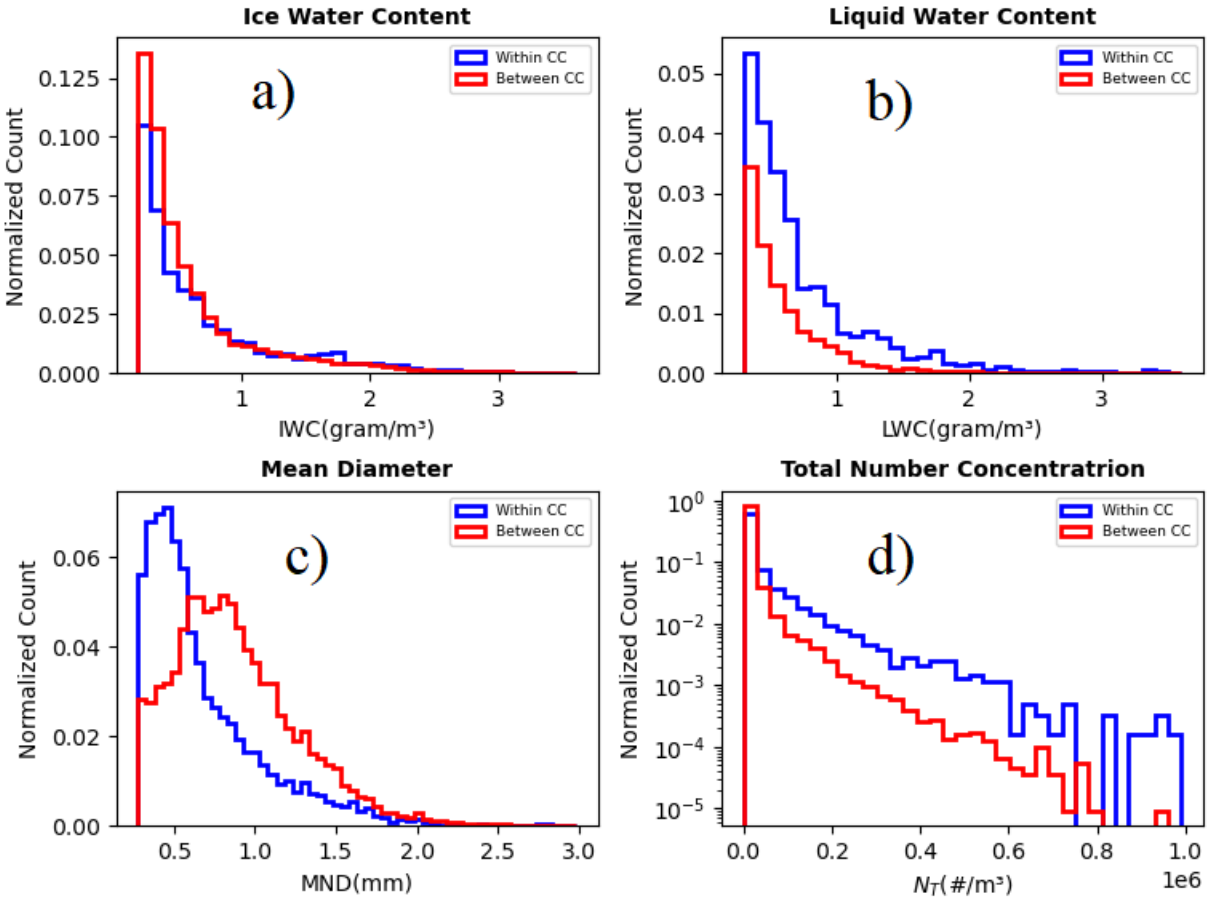

Figure 12: Normalized distribution function of IWC (a), LWC (b), MND (c), and Total Number Concentration (N_t) (d) for segments of cloud within (blue) and between (red) CC.

Date	TAMMS	RICE	CRS	2DS	HVPS	FCDP
Jan 12 2020	18:25:58-22:05:20					
Jan 18 2020	18:01:40-00:03:00			18:00:00-00:02:00	18:00:00-00:02:00	18:00:00-00:02:00
Jan 25 2020	18:53:18-00:28:21	18:36:04-00:29:04	18:19:55-00:32:01	18:52:00-00:28:00	18:52:00-00:28:00	18:52:00-00:28:00
Feb 01 2020	11:31:30-15:39:07	11:08:50-15:40:40	11:33:23-15:55:05	11:31:00-15:39:00	11:31:00-15:39:00	11:31:00-15:39:00
Feb 05 2020	18:30:43-01:39:30	18:14:00-01:40:31	19:23:25-00:49:25	18:30:00-01:39:00	18:30:00-01:39:00	18:30:00-01:39:00
Feb 07 2020	14:06:35-20:00:17	13:49:55-20:01:47	12:22:28-18:01:09	14:06:00-20:00:00	14:06:00-20:00:00	14:06:00-20:00:00
Feb 13 2020	06:23:20-12:40:25	05:48:13-12:41:16		06:13:00-12:40:00	06:13:00-12:40:00	06:13:00-12:40:00
Feb 18 2020	17:22:13-22:13:45	17:03:36-22:14:48		17:22:00-22:13:00	17:22:00-22:13:00	17:22:00-22:13:00
Feb 20 2020	19:39:42-01:11:03	19:21:19-01:11:49		19:40:00-01:11:00	19:40:00-01:11:00	19:40:00-01:11:00
Feb 24 2020	17:51:11-19:28:35	17:34:08-19:29:42		17:51:00-19:32:00	17:51:00-19:32:00	17:51:00-19:32:00
Feb 25 2020	20:58:28-04:11:04	20:35:43-04:12:00	20:29:27-03:11:41			20:58:00-04:11:00
Feb 27 2020			07:43:51-14:23:21			

Table 1: Instrument Availability. All times in GMT. Time periods where scientific quality data were available for indicated cloud probes as a function of flight day.

References

AMS, 2022: "Generating Cell" *Glossary of Meteorology*, American Meteorological Society, Accessed 15 June 2023, https://glossary.ametsoc.org/wiki/Generating_cell.

Barrick, J. D. W., J. A. Ritter, C. E. Watson, M. W. Wynkoop, J. K. Quinn, and D. R. Norfolk, 1996: Calibration of NASA Turbulent Air Motion Measurement System, 24 pp, https://ntrs.nasa.gov/api/citations/19970010469/downloads/19970010469.pdf.

Brechner, P., G. M. McFarquhar, A. Schwarzenboeck, and A. V. Korolev, 2023: Ice Crystal Size Distributions in Tropical Mesoscale Convective Systems in the Vicinity of Darwin, Australia: Results from the HAIC/HIWC Campaign, *Journal of the Atmospheric Sciences*, **80**(9), 2147–2164, https://doi.org/10.1175/jas-d-22-0209.1.

Cober, S. G., G. A. Isaac, A. V. Korolev, and J. W. Strapp, 2001: Assessing Cloud-Phase Conditions, *Journal of Applied Meteorology*, **40**(11), pp. 1967–1983, https://doi.org/10.1175/1520-0450(2001)040<1967:ACPC>2.0.CO;2.

Cronce, M., R. M. Rauber, K. R. Knupp, B. F. Jewett, J. T. Walters, and D. Phillips, 2007: Vertical motions in precipitation bands in three Winter Cyclones, *Journal of Applied Meteorology and Climatology*, **46**(10), 1523–1543, https://doi.org/10.1175/jam2533.1.

Douglas, R. H., K. L. S. Gunn, and J. S. Marshall, 1957: Pattern in the Vertical of Snow Generation, *Journal of Meteorology*, **14**(2) 95–114, https://doi.org/10.1175/1520-0469(1957)014<0095:PITVOS>2.0.CO;2.

Heymsfield, A., M. Szakáll, A. Jost, I. Giammanco, and R. Wright, 2018: A Comprehensive Observational Study of Graupel and Hail Terminal Velocity, Mass Flux, and Kinetic Energy, *Journal of the Atmospheric Sciences*, **75**(11), 3861–3885, https://doi.org/10.1175/jas-d-18-0035.1.

Kalesse, H., P. Kollias, and W. Szyrmer, 2013: On Using the Relationship between Doppler Velocity and Radar Reflectivity to Identify Microphysical Processes in Midlatitudinal Ice Clouds, *Journal of Geophysical Research: Atmospheres*, **118**(21), https://doi.org/10.1002/2013jd020386.

Kumjian, M. R., S. A. Rutledge, R. M. Rasmussen, P. C. Kennedy, and M. Dixon, 2014: High-Resolution Polarimetric Radar Observations of Snow-Generating Cells, *Journal of Applied Meteorology and Climatology*, **53**(6), 1636–1658, https://doi.org/10.1175/jamc-d-13-0312.1.

Langleben, M. P., 1956: The Plan Pattern of Snow Echoes at the Generating Level, *Journal of Meteorology*, **13**(6), 554–560, https://doi.org/10.1175/1520-0469(1956)013<0554:TPPOSE>2.0.CO;2.

Lawson, P. R., D. O'Connor, P. Zmarzly, K. Weaver, B. Baker, Q. Mo, and H. Jonsson, 2006: The 2D-S (STEREO) PROBE: Design and Preliminary Tests of a New Airborne, High-Speed, High-Resolution Particle Imaging Probe, *Journal of Atmospheric and Oceanic Technology*, **23**(11), 1462–1477, https://doi.org/10.1175/jtech1927.1.

Leroy, D., E. Fontaine, A. Schwarzenboeck, and J. W. Strapp, 2016: Ice Crystal Sizes in High Ice Water Content Clouds. Part I: On the Computation of Median Mass Diameter from in Situ Measurements, *Journal of Atmospheric and Oceanic Technology*, **33**(11), 2461–2476, https://doi.org/10.1175/jtech-d-15-0151.1

Ludlam, F. H., 1956: The Forms of Ice Clouds: II, *Quarterly Journal of the Royal Meteorological Society*, **82**(353), 257–265, https://doi.org/10.1002/qj.49708235302.

Marchand, R., and Coauthors, 2014: The Southern Ocean Clouds, Radiation, Aerosol Transport Experimental Study, 30, https://atmos.uw.edu/~roj/nobackup/Southern_Ocean_Workshop_2014/Southern_Ocean_Workshop_2014_White_Paper.pdf.

Market, P. S., K. Crandall, and R. Rauber, 2012: High-Resolution Rawinsonde Observations of The Cold-Sector Precipitation Regions in Transient Mid-Latitude Extratropical Cyclones, *National Weather Digest*, **36**(1), 3–8.

Marshall, J. S., 1953: Precipitation trajectories and patterns, *Journal of Meteorology*, **10**(1), 25–29, https://doi.org/10.1175/1520-0469(1953)010<0025:PTAP>2.0.CO;2.

McMurdie, L. A., J. A. Finlon, G. M. Heymsfield, and J. E. Yorks, 2022: Investigation of Microphysics and Precipitation for Atlantic Coast Threatening Snowstorms (IMPACTS): The 2022 Deployment, *IGARSS 2022 - 2022 IEEE International Geoscience and Remote Sensing Symposium*, Kuala Lumpur, Malaysia, 4461–4464, https://doi.org/10.1109/igarss46834.2022.9883693.

McFarquhar, G. M., and Coauthors, 2017: Processing of Ice Cloud In-Situ Data Collected by Bulk Water, Scattering, and Imaging Probes: Fundamentals, Uncertainties, and Efforts Toward Consistency. *Meteorological Monographs*, **58**, 11.1–11.3, https://doi.org/10.1175/AMSMONOGRAPHS-D-16-0007.1.

McFarquhar, G. M., and Coauthors, 2011: Indirect and semi-direct aerosol campaign: The Impact of Arctic Aerosols on Clouds. *Bulletin of the American Meteorological Society*, **92**(2), 183–201, https://doi.org/10.1175/2010BAMS2935.1.

McFarquhar, G. M., G. Zhang, M. R. Poellot, G. L. Kok, R. McCoy, T. Tooman, A. Fridlind, and A. J. Heymsfield, 2007: Ice properties of single-layer stratocumulus during the Mixed-Phase Arctic Cloud Experiment: 1. Observations, *Journal of Geophysical Research*, **112**(D24), 1–1, https://doi.org/10.1029/2007JD008633.

Murphy, A. M., R. M. Rauber, G. M. McFarquhar, J. A. Finlon, D. M. Plummer, A. A. Rosenow, and B. F. Jewett, 2016: A Microphysical Analysis of Elevated Convection in the Comma Head Region of Continental Winter Cyclones, *Journal of the Atmospheric Sciences*, **74**(1), 69–91, https://doi.org/10.1175/jas-d-16-0204.1.

Plummer, D. M., G. M. McFarquhar, R. M. Rauber, B. F. Jewett, and D. C. Leon, 2014: Structure and Statistical Analysis of The Microphysical Properties of Generating Cells in The Comma Head Region of Continental Winter Cyclones, *Journal of the Atmospheric Sciences*, **71**(11), 4181–4203, https://doi.org/10.1175/JAS-D-14-0100.1.

Plummer, D. M., G. M. McFarquhar, R. M. Rauber, B. F. Jewett, and D. C. Leon, 2015: Microphysical Properties of Convectively Generated Fall Streaks Within the Stratiform Comma Head Region of Continental Winter Cyclones, *Journal of the Atmospheric Sciences*, **72**(6), 2465–2483, https://doi.org/10.1175/JAS-D-14-0354.1.

Rauber, R. M., and Coauthors, 2014: Stability and Charging Characteristics of the Comma Head Region of Continental Winter Cyclones, *Journal of the Atmospheric Sciences*, **71**(5), 1559–1582, https://doi.org/10.1175/jas-d-13-0253.1.

Robusto, C. C., 1957: The Cosine-Haversine Formula, *The American Mathematical Monthly*, **64**(1), 38–40, https://doi.org/10.2307/2309088.

Rosenow, A. A., D. M. Plummer, R. M. Rauber, G. M. McFarquhar, B. F. Jewett, and D. Leon, 2014: Vertical Velocity and Physical Structure of Generating Cells and Convection in the Comma Head Region of Continental Winter Cyclones, *Journal of the Atmospheric Sciences*, **71**(5), 1538–1558, https://doi.org/10.1175/jas-d-13-0249.1.

Smith, C. D., A. Ross, J. Kochendorfer, M. E. Earle, M. Wolff, S. Buisán, Y.-A. Roulet, and T. Laine, 2020: Evaluation of the WMO Solid Precipitation Intercomparison Experiment (SPICE) Transfer Functions for Adjusting the Wind Bias in Solid Precipitation Measurements, *Hydrol. Earth Syst. Sci.*, **24**, 4025–4043, https://doi.org/10.5194/hess-24-4025-2020.

Su, C.-L., Y.-H. Chu, and I.-Y. Lo, 2009: Negative Correlation between Terminal Velocity and VHF Radar Reflectivity: Observation and Plausible Explanation, *Annales Geophysicae*, **27**(4), 1631–1642, https://doi.org/10.5194/angeo-27-1631-2009.

Varcie, M. M., 2021: Precipitation growth processes in the comma head region of an East Coast winter storm, M.S. thesis, Department of Atmospheric Sciences, Graduate College of the University of Illinois Urbana-Champaign, 78 pp.

Walker McLinden, M. L., L. Li, G. M. Heymsfield, M. Coon, and A. Emory, 2021: The NASA GSFC 94-Ghz Airborne Solid-State Cloud Radar System (CRS), *Journal of Atmospheric and Oceanic Technology*, **38**(5), 1001–1017, https://doi.org/10.1175/jtech-d-20-0127.1.

Wang, Y., and Coauthors, 2020: Microphysical Properties of Generating Cells over the Southern Ocean: Results from Socrates, *Journal of Geophysical Research: Atmospheres*, **125**(13), https://doi.org/10.1029/2019jd032237.

Wexler, R., 1955: Radar Analysis of Precipitation Streamers Observed 25 February 1954, *Journal of Meteorology*, **12**(4), 391–393, https://doi.org/10.1175/1520-0469(1955)012<0391:RAOPSO>2.0.CO;2.

Wexler, R., and D. Atlas, 1959: Precipitation Generating Cells, *Journal of Meteorology*, **16**(3), 327–332, https://doi.org/10.1175/1520-0469(1959)016<0327:PGC>2.0.CO;2.